AGU PUBLICATIONS

JGR

Journal of Geophysical Research: Oceans

RESEARCH ARTICLE

10.1002/2016JC012319

Key Points:
- Converging (diverging) alongshore currents resulting from wave refraction over an offshore canyon cause accretion (erosion) at an onshore beach
- The incidence angle of offshore waves determines the locations of converging and diverging currents
- Bathymetric features on the inner shelf can have first-order effects on surf zone morphologic change

Correspondence to:
J. Hansen,
jeff.hansen@uwa.edu.au

Citation:
Hansen, J. E., B. Raubenheimer, S. Elgar, J. H. List, and T. C. Lippmann (2017), Physical linkages between an offshore canyon and surf zone morphologic change, *J. Geophys. Res. Oceans*, *122*, 3451–3460, doi:10.1002/2016JC012319.

Received 7 SEP 2016
Accepted 20 MAR 2017
Accepted article online 23 MAR 2017
Published online 29 APR 2017

© 2017. American Geophysical Union. All Rights Reserved.

Physical linkages between an offshore canyon and surf zone morphologic change

Jeff E. Hansen[1,2], Britt Raubenheimer[2], Steve Elgar[2], Jeffrey H. List[3], and Thomas C. Lippmann[4]

[1]Univeristy of Western Australia, School of Earth Sciences and The Oceans Institute, Crawley, Western Australia, [2]Woods Hole Oceanographic Institution, Department of Applied Ocean Physics and Enginering, Woods Hole, Massachusetts, USA, [3]United States Geological Survey, Coastal and Marine Geology Program, Woods Hole, Massachusetts, USA, [4]Center for Coastal and Ocean Mapping, University of New Hampshire, Durham, New Hampshire, USA

Abstract The causes of surf zone morphologic changes observed along a sandy beach onshore of a submarine canyon were investigated using field observations and a numerical model (Delft3D/SWAN). Numerically simulated morphologic changes using four different sediment transport formulae reproduce the temporal and spatial patterns of net cross-shore integrated (between 0 and 6.5 m water depths) accretion and erosion observed in a ~300 m alongshore region, a few hundred meters from the canyon head. The observations and simulations indicate that the accretion or erosion results from converging or diverging alongshore currents driven primarily by breaking waves and alongshore pressure gradients. The location of convergence or divergence depends on the direction of the offshore waves that refract over the canyon, suggesting that bathymetric features on the inner shelf can have first-order effects on short-term nearshore morphologic change.

1. Introduction

Changes in sandy beach morphology most often are attributed to seasonal fluctuations in incident wave height, as well as individual, or sequences of storms [*Sonu and VanBeek*, 1971; *Aubrey*, 1979; *Aubrey et al*., 1980; *Lee et al*., 1998; *Dail et al*., 2000]. Sand is transported offshore during large waves and stored in a sandbar, with subsequent onshore sandbar movement during moderate wave conditions [*Thornton et al*., 1996; *Gallagher et al*., 1998; *Hoefel and Elgar*, 2003; *Henderson et al*., 2004]. Alongshore variability in the observed evolution of nearshore morphology has been attributed to several factors, including antecedent beach morphology [*Yates et al*., 2009], underlying geology [*McNinch*, 2004], and alongshore variations in cross-shore transport [*Harley et al*., 2011]. Alongshore-variable waves and currents resulting from offshore bathymetric features, such as a dredge borrow pit [*Benedet and List*, 2008], submarine canyon [*Apotsos et al*., 2008], or ebb-tidal delta [*Shi et al*., 2011; *Hansen et al*., 2013] also may cause alongshore-variable bathymetric changes [*Bender and Dean*, 2003].

The La Jolla and Scripps submarine canyons near La Jolla, CA (Figure 1a) extend onshore to about 10 m water depth, and affect the incident wave field [*Magne et al*., 2007; *Thomson et al*., 2007] and the surf zone circulation [*Long and Özkan-Haller*, 2005; *Apotsos et al*., 2008; *Hansen et al*., 2015; *Long and Özkan-Haller*, 2016]. In particular, refraction of incident waves over the submarine canyon introduces large alongshore gradients in the wave field (up to a factor of four difference in wave height over 450 m [*Apotsos et al*., 2008]), which leads to alongshore-variable forcing. Numerical simulations onshore of Scripps Canyon (Figure 1) show that the surf zone wave and depth-averaged alongshore momentum balance primarily is between the sum of the pressure and radiation-stress gradients and the sum of the total acceleration and bottom stress [*Hansen et al*., 2015]. The alongshore-variable forcing leads to alongshore currents that either converge or diverge between about alongshore coordinate $y = 1450$ and 1750 m (Figure 1b) [*Long and Özkan-Haller*, 2005; *Apotsos et al*., 2008; *Hansen et al*., 2015; *Long and Özkan-Haller*, 2016]. Here, observed alongshore-variable morphologic changes are linked to these converging or diverging alongshore currents.

2. Observations

Observations of water levels, waves, and currents were made near La Jolla, CA for approximately 7 weeks during October and November 2003 at 26 sites along the 1.0, 2.5, and 5.0 m depth contours, forming nine

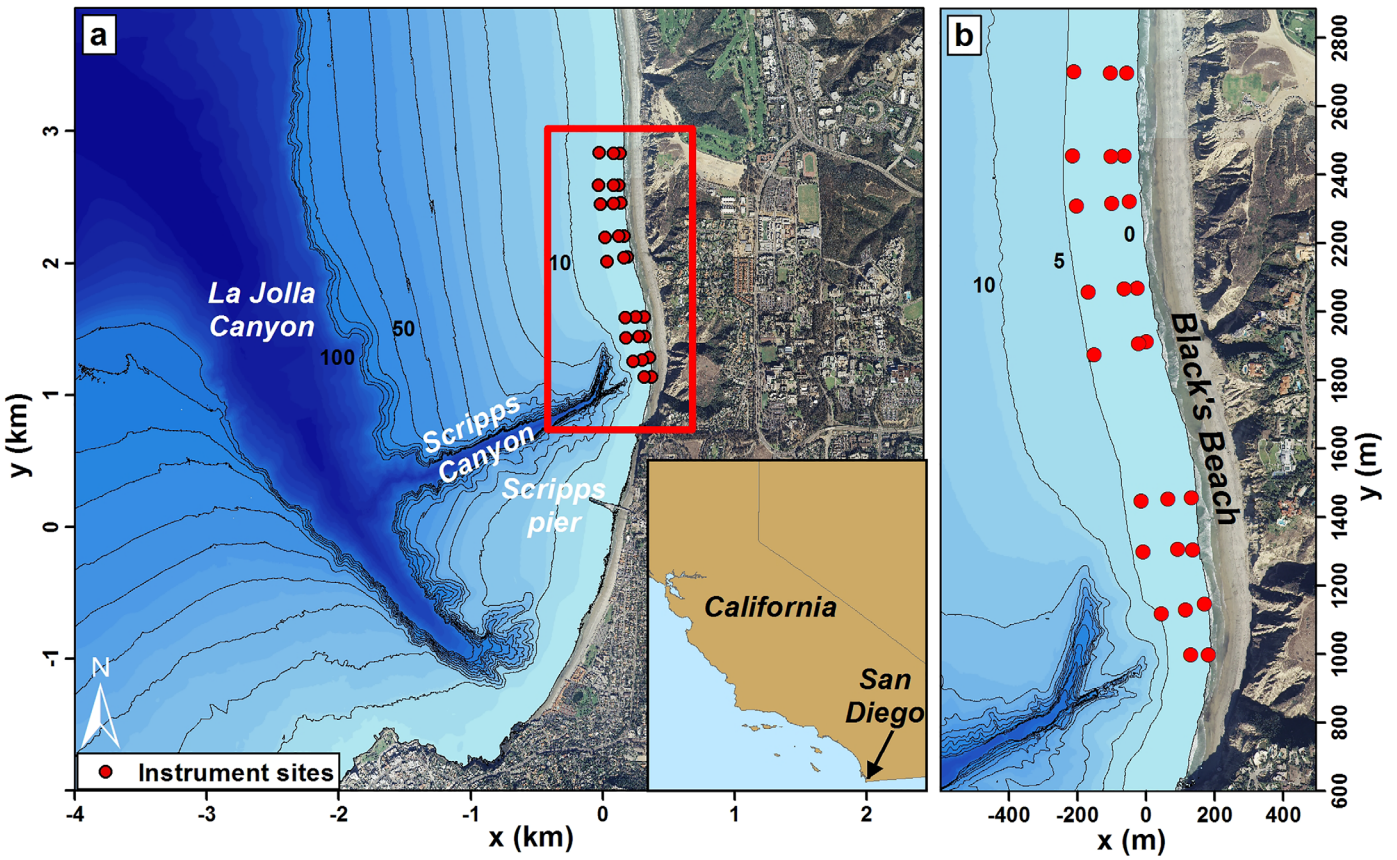

Figure 1. (a) Map showing La Jolla and Scripps submarine canyons (black curves are depth contours every 10 m from 10 to 100 m) near San Diego, CA (location shown in inset), as well as the study area (red box) and instrument sites (red circles). (b) Instrument sites (red circles) along the 1.0, 2.5, and 5.0 m depth contours. The local coordinate system is relative to the Scripps pier (visible in Figure 1a). Adapted from *Hansen et al.* [2015].

cross-shore transects [*Apotsos et al.*, 2008] (Figure 1). Acoustic Doppler velocimeters (ADV) were located 0.3, 0.3, and 0.6 m above the bed for the 1, 2.5, and 5 m sites, respectively. Pressure sensors were buried 0.5 m below sand level at the 1 and 2.5 m sites, and were located 0.5 m above sand level at the 5 m sites. The ADVs and pressure sensors were sampled at 2 or 16 Hz for 51.2 min every hour. Offshore wave heights, periods, and directions (Figure 2) were estimated with observations from a WaveRider buoy approximately 15 km NW of the experiment area in 550 m depth (http://cdip.ucsd.edu/?nav=recent&xitem=info&stn=100&stream=p1). Frequency-directional wave spectra were estimated every 30 min using the maximum entropy method [*Lygre and Krogstad*, 1986]. Wind was recorded at the end of Scripps pier (Figure 1a).

Beach and nearshore morphology was surveyed from the bluff base to between 6 and 8 m depth every 25–50 m alongshore approximately weekly with a Differential Global Positioning System (DGPS) receiver mounted on an ATV or push dolly (on the subaerial beach) and with a DGPS, gyrometer, and single-beam echo-sounder mounted on a personal-watercraft [*Lippmann and Smith*, 2009]. Points from each survey were used to construct a triangulated-irregular-network surface elevation model that was interpolated onto a 2 $\times$ 2 m grid. Control points were not sampled before and after each survey. Thus, small offsets (less than 0.10 m, and typically about 0.05 m) were added or removed to all points in each gridded survey assuming sand was conserved within the survey region (zero net volume change). Resulting differences in elevation between successive grids were used to estimate the spatially varying sand volume changes. Outside the area covered by the weekly surveys, bathymetry and topography is from a U.S. Geological Survey Digital Elevation Model [*Barnard and Hoover*, 2010] and NOAA National Ocean Service surveys.

Topobathymetric surveys on 6 and 13 October show that a 1.5 m high "wedge" of accretion formed between alongshore distances $y = 1450$ and 1750 m in $\sim$3 m (initial) depth (Figure 3a) during a period with $\sim$1.2 m high, 10 s waves from the WNW (Figure 2). In contrast, surveys on 27 and 30 October suggest the wedge area eroded, and the sandbar moved onshore (Figure 4a) during a period with 0.6 m high, 17 s

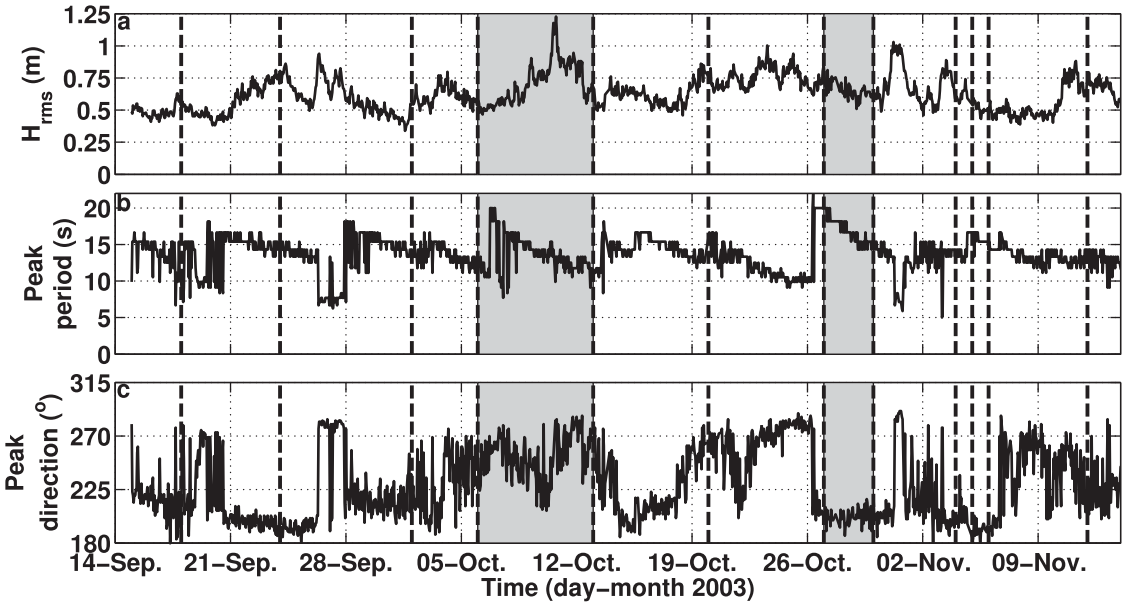

Figure 2. (a) Wave height (H_{rms}), (b) peak period, and (c) peak direction estimated with observations from a buoy in 550 m water depth versus time. The gray areas are 6–13 October and 27–30 October, discussed in the text, and the vertical-dashed lines indicate the dates of the topobathymetric surveys.

waves from the SSW (Figure 2). For safety of surfers, there were no wave or current measurements collected in the region of the maximum bathymetric change (Figure 1b, $1500 < y < 1750$ m). Thus, numerical morphodynamic simulations are used to examine the role of converging or diverging alongshore currents in net cross-shore profile volume change.

3. Numerical Model

Nearshore waves, circulation, and sediment transport were simulated from 6 to 13 October (accretion, Figure 3) and from 27 to 30 October (erosion, Figure 4) with the numerical model Delft3D [*Lesser et al*., 2004] coupled with the phase-averaged wave model SWAN [*Booij et al*., 1999]. Here, the circulation and wave models (described in *Hansen et al*. [2015]) are combined with sediment transport and morphologic change calculations.

3.1. Coupled Wave and Circulation Model

Waves were simulated over several nested SWAN model domains, while water levels, currents, and sediment transport were simulated using two Delft3D flow domains. The largest wave domain extends offshore of the continental shelf [*Gorrell et al*., 2011; *Hansen et al*., 2015], and stationary SWAN simulations are driven every 20 min with frequency-directional spectra estimated from wave buoy measurements (interpolated from the 30 min observations). Tidal boundary conditions for the two curvilinear shoreline-following hydrodynamic domains are provided using a combination of Neumann (depths < 5 m) and Riemann (depths > 5 m) boundary conditions from a larger "tide" model that is forced with satellite-derived, spatially variable astronomic tidal constituents (without surface gravity waves) [*Hansen et al*., 2015]. The SWAN wave energy output along the seaward boundaries of the hydrodynamic domains, and the SWAN-simulated mean direction and peak frequency at each cell, are used to drive the Delft3D roller module that solves the short-wave energy balance [*Reniers and Battjes*, 1997]. The Delft3D circulation model is run in depth-averaged mode (2DH) with a 1.5 s time step on the two domains, which are two-way coupled via domain decomposition and coupled with the wave model [*Hansen et al*., 2015]. The spatial resolution of the model domains is approximately 4×8 m in the cross and alongshore directions, respectively, near the shoreline, and decreases offshore to about 15×20 m for the flow model, and to 300×700 m for the coarsest wave domain [*Hansen et al*., 2015]. Surveyed bathymetry and topography were linearly interpolated onto the numerical domain grids. The total horizontal eddy viscosity in each grid cell is the sum of the background

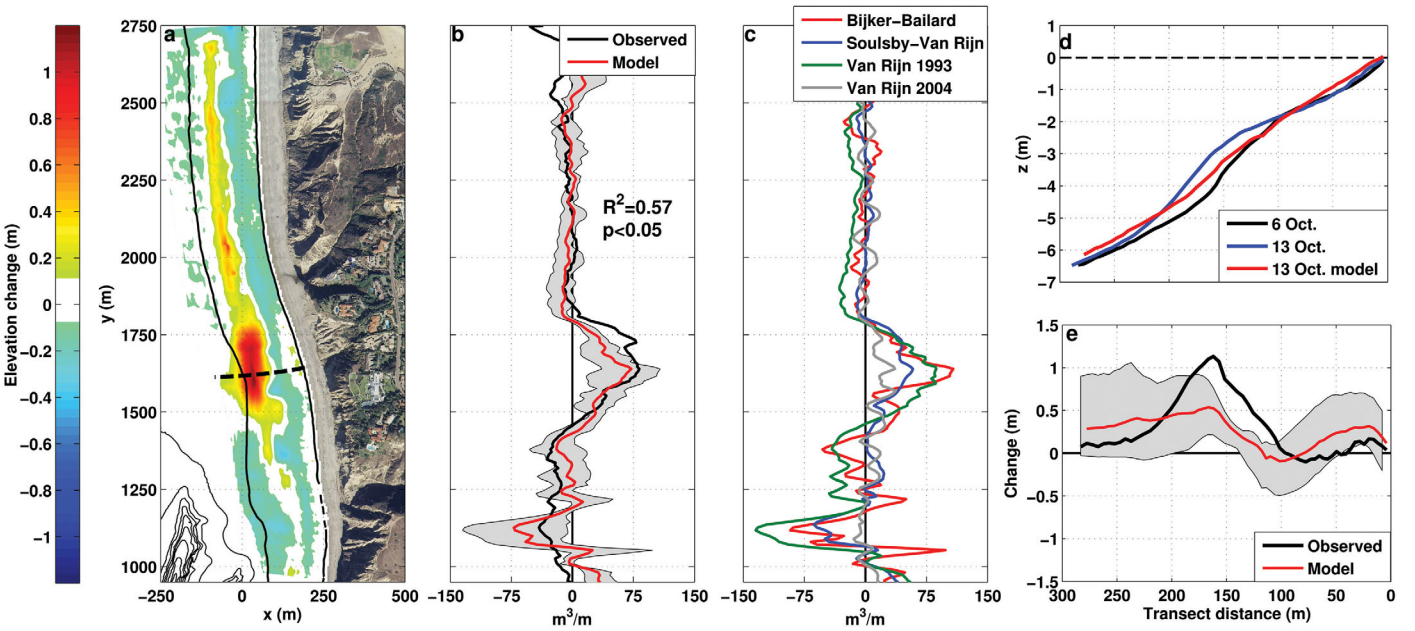

Figure 3. (a) Contours of elevation change between 6 and 13 October (color scale on left, changes less than 0.08 m not shown) as a function of cross and alongshore position. The thin black curves are depth contours at 0, 5, and every 10 m from 10 to 100 m for the 6 October bathymetry. (b) Observed (black) and ensemble simulated (red) cross-shore integrated (0–6.5 m depth) profile volume change (grey area indicates range across the four formulae). (c) Simulated cross-shore integrated profile volume change from each of the four transport formulae. (d) Seafloor elevation versus cross-shore distance at $y = 1640$ m (dashed black curve in Figure 3a, which passes through the area of largest bathymetric change) observed on 6 (black curve) and 13 (blue) October and simulated (ensemble) on 13 October (red). (d) Observed (black curve) and simulated (ensemble) (red) depth changes between the transects shown in Figure 3d versus cross-shore distance (grey shading is the range of the four formulae).

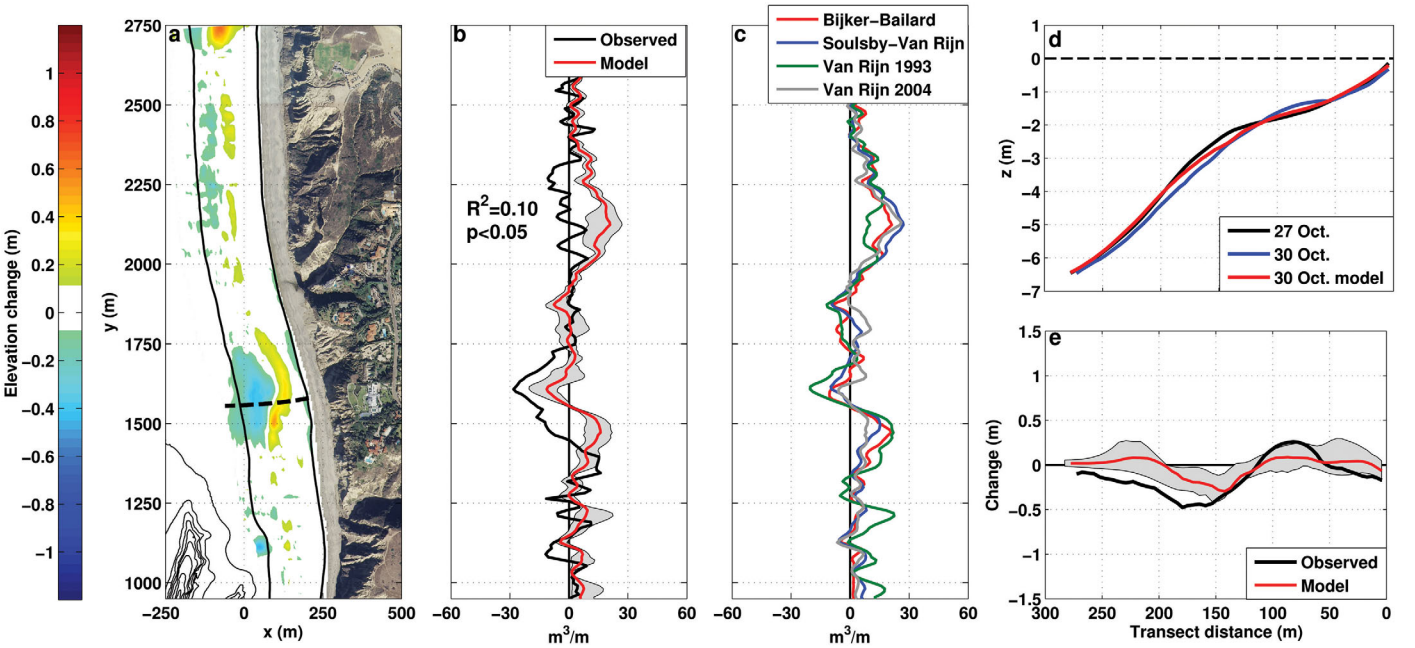

Figure 4. (a) Contours of elevation change between 27 and 30 October (color scale on left, changes less than 0.08 m not shown) as a function of cross and alongshore position. The thin black curves are depth contours at 0, 5, and every 10 m from 10 to 100 m for the 27 October bathymetry. (b) Observed (black) and ensemble simulated (red) cross-shore integrated (0–6.5 m depth) profile volume change (grey area indicates range across the four formulae). (c) Simulated cross-shore integrated profile volume change from each of the four transport formulae. (d) Seafloor elevation versus cross-shore distance at $y = 1640$ m (dashed black curve in Figure 4a, which passes through the area of largest bathymetric change] observed on 27 (black curve) and 30 (blue) October and simulated (ensemble) on 30 October (red). (d) Observed (black curve) and simulated (ensemble) (red) depth changes between the transects shown in Figure 4d versus cross-shore distance (grey shading is the range of the four formulae).

horizontal eddy viscosity (0.5 m^2/s) [*Hansen et al.*, 2015] and a turbulent eddy viscosity based on the wave roller dissipation [*Battjes*, 1975]. A Chezy (C_z) roughness of 70 $m^{0.5}/s$ (equivalent to a drag coefficient, C_d, of 0.002) is applied in both the cross and alongshore directions. Simulations of waves [*Gorrell et al.*, 2011] and currents [*Hansen et al.*, 2015, which includes additional model details] have been compared with observations in this area (at the sensors in the red box in Figure 1).

3.2. Sediment Transport Formulae

The total sediment transport (the sum of bed and suspended load) is estimated using four different noncohesive transport formulae available within Delft3D, including a modified version of *Van Rijn* [1993] (the default in Delft3D), *Bijker* [1971] with transport owing to wave asymmetry following *Bailard* [1981], *Soulsby* [1997] (*Soulsby-Van Rijn* method), and *Van Rijn et al.* [2004]. Although there are additional transport formulae available within Delft3D, the four formulations included here specifically include the effect of waves on sediment transport via parameterizations for increased sediment suspension due to the presence of waves, as well as transport due to wave nonlinearity. For a complete description of the formulations, see the original references, as well as the Delft3D Flow user manual (http://oss.deltares.nl/web/delft3d/manuals). The coefficients in the transport formulae were not tuned to match the observed morphologic changes, and no attempt was made to reproduce changes in the subaerial beach. Each formulation was used with default settings and coefficients (when available), or with coefficients based on previously published literature or technical reports, or on physical characteristics of the site (e.g., grain size) (Table 1). Sediment in the model was specified as noncohesive sand with a median diameter (D50) of 0.22 mm, consistent with sand sampled at the study site (Table 1).

Altering the coefficients and parameters within the overall model and within each formulation may change the magnitude of the simulated transport and resulting morphologic changes, but has a limited effect on the simulated alongshore transport patterns examined here. The coefficients specific to each transport formulae (Table 1) predominantly influence the amount of transport in the direction of wave propagation (which is near shore-normal within the surf zone) and thus impact, for example, the cross-shore evolution of sand bars. The bathymetric change within each grid cell at each computational step is calculated by computing the change in sediment mass resulting from sources, sinks (e.g., sediment suspension and deposition), and transport gradients. The change in mass is converted to an elevation change by using a dry bed density of 1600 kg/m^3 (Table 1) [*Lesser et al.*, 2004]. Owing to feedback with the morphology, the wave and current fields are slightly different for each sediment transport formula

Table 1. Constants and Empirical Parameters Used for Each of the Four Transport Formulae

Universal Values	
Horizontal eddy diffusivity (m^2/s)	10
Median sediment diameter (mm)	0.22
Sediment density (kg/m^3)	2650
Dry bed density (kg/m^3)	1600
Sediment thickness (m)	5
Morphologic scale factor	1
Factor for erosion of adjacent dry cells	0.33
Van Rijn [1993][a]	
Wave-related suspended transport factor	0.4
Wave-related bed load transport factor	0.4
Van Rijn et al. [2004][a]	
Wave-related suspended transport factor	0.4
Wave-related bed load transport factor	0.4
Soulsby [1997] (Soulsby-Van Rijn)	
Calibration coefficient	1.5
D90/D50 grainsize ratio	1.5
Roughness height (m)	0.01
Bijker [1971] with *Bailard* [1981]	
Bijker [1971] parameters	
Coefficient for shallow water	5
Coefficient for deep water	2
Shallow water limit (H_{sig}/h)	0.05
Deep water limit	0.2
D90 grainsize (mm)	0.3
Bottom roughness height for currents (m)	0.05
Particle fall velocity (m/s)	0.16
Porosity	0.4
Wave period (s)	9
Bailard [1981] parameters[b]	
Calibration coefficient for wave asymmetry	0.4
Calibration coefficient for average flow	0
General calibration coefficient (ε)	0.11

[a]Remaining parameters default (see Delft3-D Flow manual).
[b]From *Nipius* [1998].

The surf zone cross-shore integrated (0–6.5 m depth) profile volume changes observed between 6 and 13 October and between 27 and 30 October are compared with the cross-shore integrated profile volume changes from the four transport-formulae, and with the ensemble average of the four formulae. Although the transport and morphologic change patterns simulated by the four transport formulae are similar for both periods, ensemble averaging reduces the sensitivity of the results to the settings of any one formula (Figures 3b and 4b).

4. Simulated Morphologic Changes

4.1. Accretion of the "Wedge" 10 October 2003

Conditions between the 6 and 13 October surveys included a ~24 h wave event on 10 October with ~1.2 m H_{rms}, 10 s waves from the WNW (Figure 2). The numerical model, initialized with the bathymetry observed on 6 October, was run from 6 to 13 October using each transport formula. The 7 day ensemble-averaged velocity field indicates converging alongshore flows at $y \sim 1600$ m (Figure 5a), consistent with a visually observed rip-current [*Long and Özkan-Haller*, 2005] and with the location of the "wedge" ($1450 < y < 1750$ m, Figure 3a). This converging flow pattern persisted throughout the 7 day period (with the magnitude fluctuating with the offshore wave height) and resulted from an alongshore-variable imbalance between the pressure-gradient forcing and the radiation-stress forcing (Figure 6). Wave energy (and wave-driven setup) was maximum in the "wedge region" because waves that propagated over Scripps Canyon were refracted toward the north (approached the beach from the WSW) and interacted with waves from the WNW that did not propagate over the canyon. Thus, the radiation-stress forcing is toward the south (from WNW waves) north of the flow convergence and wedge area ($1600 < y < 2000$ m) and toward the north (from the refracted waves) south ($1200 < y < 1500$ m) of the flow convergence, whereas the alongshore pressure gradient exhibits the opposite trend (Figure 6). The simulated profile volume changes from the four transport formulae and their ensemble-average indicate accretion in the same location as the observed wedge, but with a smaller magnitude than observed ($1450 < y < 1750$ m, Figures 3b and 3c). Despite the differences in the magnitudes of the simulated and observed profile volume changes (which might be improved with model tuning), the alongshore pattern of the observed profile volume change is

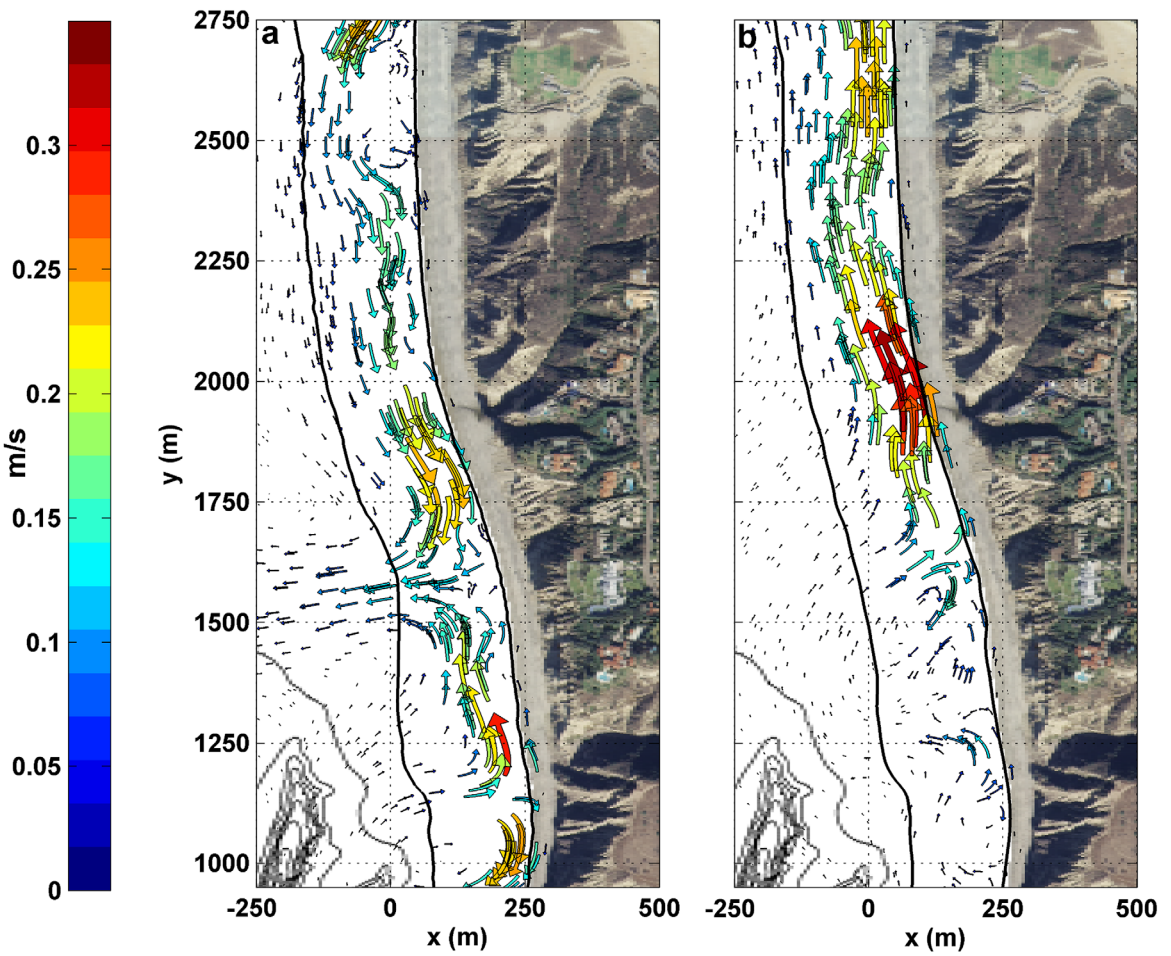

Figure 5. (a) Generalized Lagrangian Mean velocity vectors ensemble averaged across the four model runs with the different transport formulae as a function of cross and alongshore position for (a) 6–13 October and (b) 27–30 October. Arrows point in direction of flow, with lengths proportional to speed, which also is given by the arrow color (color scale on left). The thin black curves are depth contours at 0, 5, and every 10 m from 10 to 100 m.

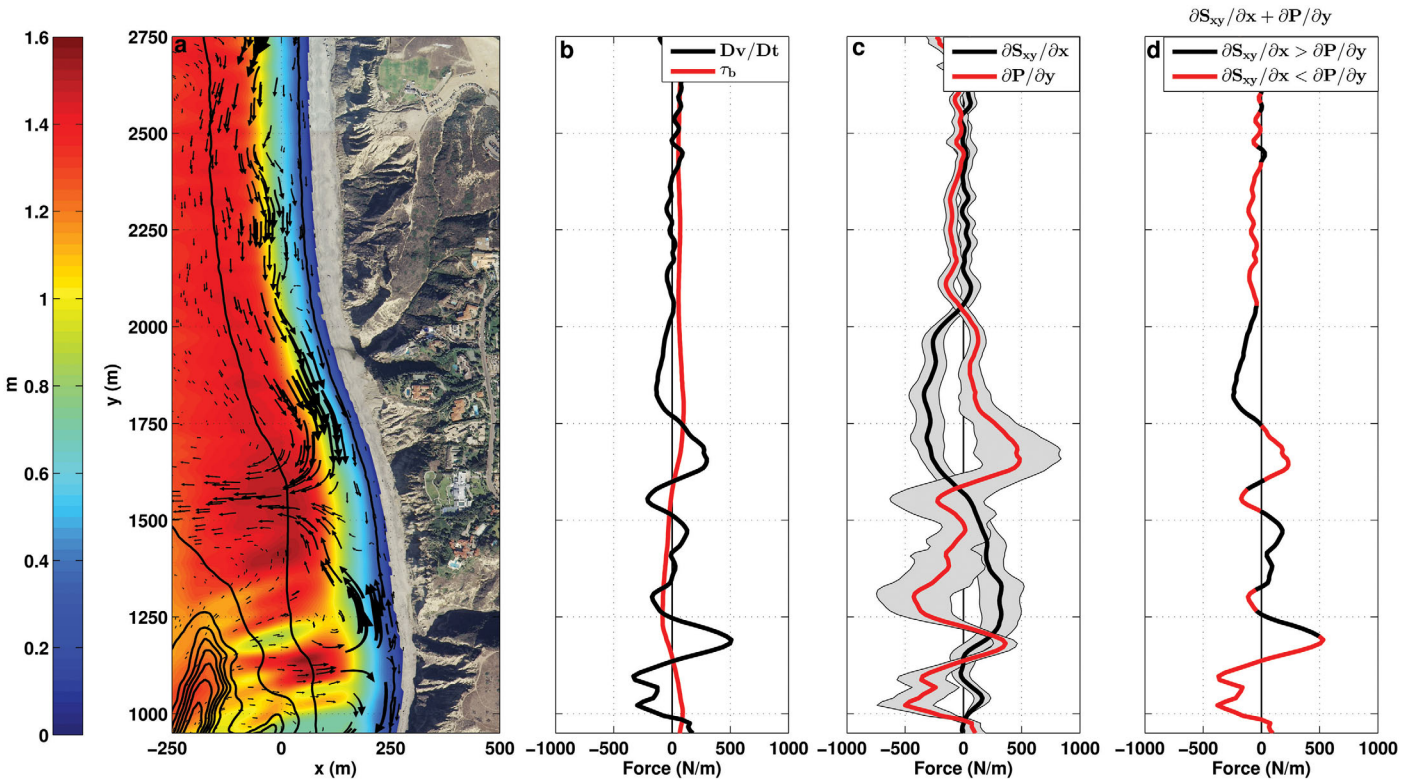

Figure 6. (a) Simulated significant wave height (color, scale to left) and generalized Lagrangian mean velocity vectors (black arrows) averaged over the 24 h period encompassing the high wave event on 10 October (Figure 2). The thin black curves are depth contours at 0, 5, and every 10 m from 10 to 100 m. Alongshore structure of cross-shore integrated (0–6.5 m depth) and 24 h averaged (b) total acceleration (*Dv/Dt*, sum of local acceleration and nonlinear advective terms, black) and bottom stress (red), (c) radiation-stress (black), and alongshore pressure (red) gradients, with gray shading indicating ±1 standard deviation over the 24 h period, and (d) sum of the pressure and radiation-stress gradients. In Figure 6d, the color indicates which forcing term is larger (black is radiation-stress gradient > pressure gradient, red is pressure gradient > radiation-stress gradient).

reproduced (Figure 3). The net accretion of the cross-shore profile (Figures 3b and 3c) resulted from the converging alongshore surf zone flows (Figure 5a) and from net sediment delivery from both up and down coast to the area between $y = 1450$ and 1750 m. The model results also suggest that the strongest alongshore flows (up to 0.8 m/s), transport, and convergence occurred in 1–2 m depth (Figure 5a), and that an offshore-directed current (exceeding 0.5 m/s) may have carried sediment offshore to 3–5 m depth (based on the initial 6 October bathymetry) (Figure 3a). Offshore H_{rms} was greater than 0.8 m for ~3.25 days during the wave event, and in the simulations the wedge area accreted continuously during the 7 days between surveys, with significant expansion in both the cross and alongshore directions surrounding the period of elevated waves on 10 October (Figure 2).

4.2. Erosion Event 27 October 2003

Wave conditions between the 27 and 30 October surveys consisted primarily of 17 s SSW swell, with $0.5 < H_{rms} < 0.8$ m (Figure 2). Over the 3 day period, the bathymetry for $1450 < y < 1750$ m eroded in >2 m depth and accreted between 1 and 2 m depths (Figure 4a). The observations suggest onshore transport of some sediment, with net erosion of the subaqueous cross-shore profile between 0 and 6.5 m depths for $1450 < y < 1750$ m (Figure 4b). The ensemble-averaged simulated velocity field indicates alongshore flows diverged in this region (Figure 5b), owing primarily to an imbalance between northerly directed radiation-stress gradients (which dominate for $1600 < y < 1850$ m) and southerly directed pressure gradients (which dominate for $1400 < y < 1650$ m) [*Apotsos et al.*, 2008 (observations); *Hansen et al.*, 2015 (simulations)]. The simulated northerly alongshore flows reached ~0.5 m/s north of the divergence region, and maximum southerly flows were ~0.2 m/s south of the divergence (Figure 5b). The diverging alongshore currents resulted in onshore-directed mean flows in the wedge area (Figure 5b) and net erosion of the cross-shore profile (Figure 4b). Similar to the 6 to 13 October period, the model underestimates the magnitude of the profile volume change and, in this case, the alongshore extent (Figures 4b and 4c). The observed elevation

changes (Figure 4a) indicate onshore migration of some sediment, which is not simulated accurately by the 2DH model (Figures 4d and 4e).

5. Discussion

Convergences and divergences of the alongshore flows at this site are owing primarily to refraction of waves propagating over the submarine canyon, resulting in alongshore-variable wave heights and wave directions outside the surf zone [*Long and Özkan-Haller*, 2005; *Apotsos et al*., 2008; *Hansen et al*., 2015; *Long and Özkan-Haller*, 2016]. When the offshore waves approach from the WSW to WNW (incident angles $> 220°$) alongshore flows converge between $1550 < y < 1650$ m, whereas when offshore waves approach from the S to SW (incident angles $< 210°$), alongshore flows mostly diverge in this area (Figure 7a) [see also *Long and Özkan-Haller*, 2016]. The differences in the flow fields (e.g., Figure 5) result in different morphologic responses. The observed offshore peak wave direction is correlated with the net cross-shore (0–6.5 m depth) profile volume change rate between surveys ($R^2 = 0.71$, $p < 0.05$) and with the simulated velocity divergence ($R^2 = 0.62$, $p < 0.05$, calculated from hydrodynamic only simulations), both averaged over $1550 < y < 1650$ m (the center of the region that erodes or accretes, Figure 7a). The cross-shore profile volume change rate is uncorrelated with wave height ($R^2 = 0.11$, $p = 0.32$) and only weakly correlated with wave period ($R^2 = 0.39$, $p < 0.05$), which was weakly correlated with wave direction. Correspondingly, the observed net profile ($1550 < y < 1650$ m) volume change rate also is correlated ($R^2 = 0.51$, $p < 0.05$) with the simulated velocity divergence averaged over the same time and area (Figure 7b). As the offshore peak wave direction increases above ~220°, the flow convergence between $y = 1550$ and 1650 m increases, resulting in increasing accretion. When the waves approach from ~220°, there is relatively little velocity divergence and morphologic change, whereas during the period (averaged between surveys) with waves from ~200° (27–30 October), flows diverge and there is erosion.

To examine further the connection between offshore wave direction and erosion or accretion resulting from converging or diverging alongshore currents, morphologic evolution was simulated for two sets of idealized conditions. Specifically, the evolution over 72 h was simulated with each of the four transport formulae using 0.7 m H_{rms}, 15 s peak period offshore waves (JONSWAP spectrum) with directions of either 290° (WNW) or 200° (SSW) and a directional spread of 25°. Each simulation was initialized with the observed

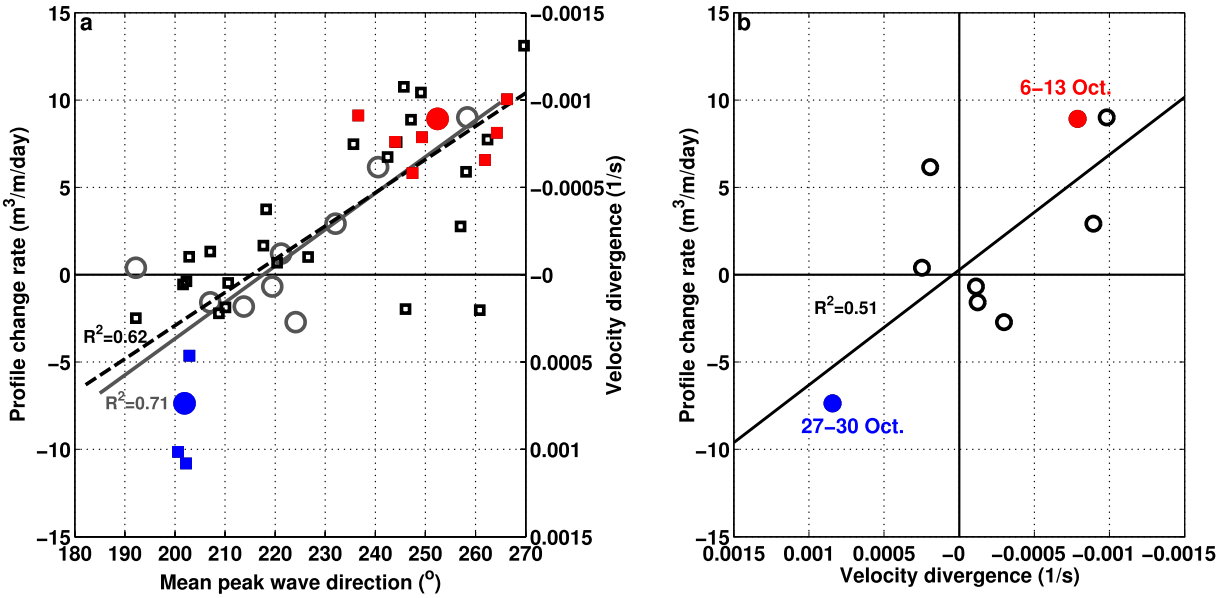

Figure 7. (a) Observed cross (0–6.5 m depth) and alongshore ($1550 < y < 1650$ m) averaged profile volume change rate between successive surveys (left axis, circles, and solid grey regression line), and daily averaged, simulated velocity divergence (right axis, squares, and dashed black regression line, note reversed scale) versus the mean peak incident wave direction recorded between the surveys. (b) Observed cross-shore profile volume change rate versus simulated cross and alongshore-averaged velocity divergence (note reversed scale), averaged over the time period between surveys. In both Figures 7a and 7b, the red symbols are from 6 to 13 October, and the blue symbols are from 27 to 30 October. The red and blue circles in Figure 7a are from the same model runs as the red and blue circles in Figure 7b. Two additional surveys from September 2013 are included in Figure 7a that were not simulated, and thus are not in Figure 7b.

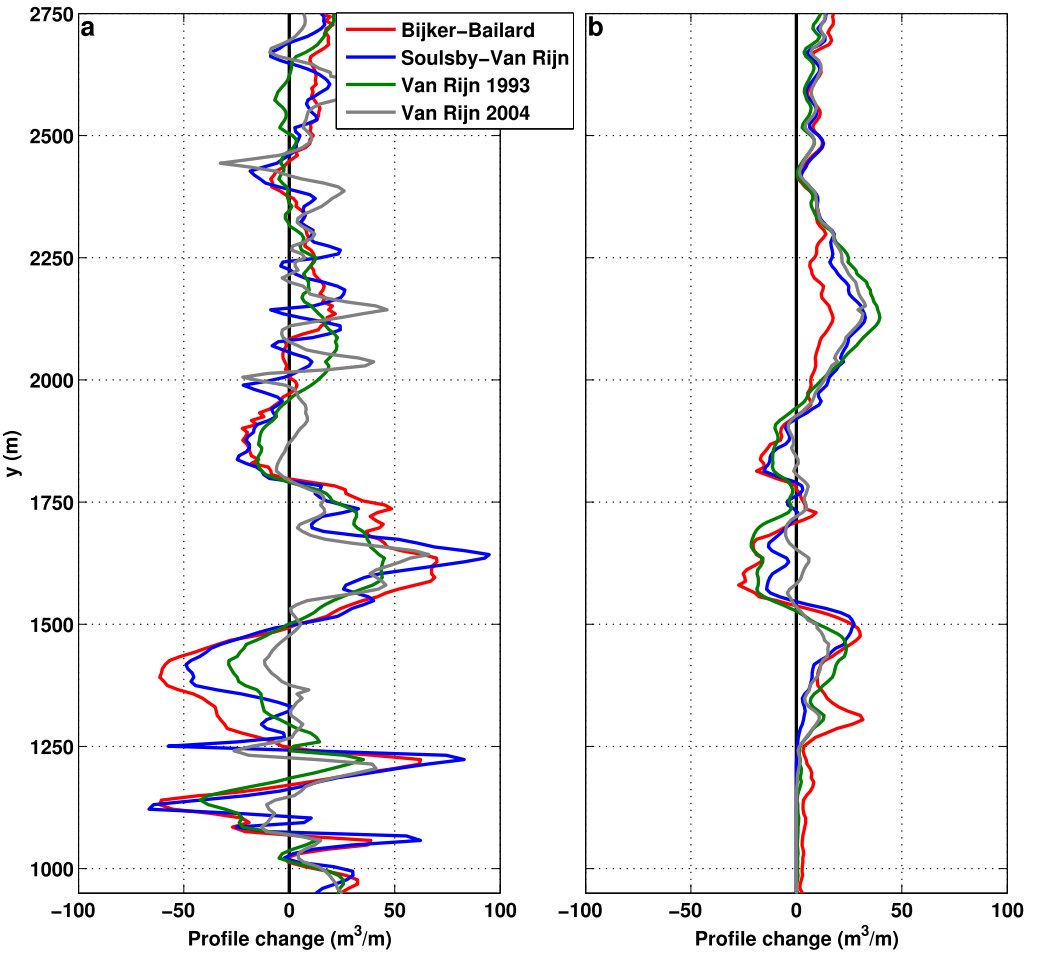

Figure 8. Cross-shore integrated (0–6.5 m depth) profile volume change per m of shoreline from each of the four transport formulae resulting from 72 h of 1 m high, 15 s peak period offshore waves with a JONSWAP spectral shape approaching from (a) 290° (WNW) or (b) 200° (SSW) with directional spread of 25°. The initial bathymetry is from 6 October for both sets of simulations.

6 October bathymetry and forced with realistic tides from 6 to 9 October. The results from the idealized simulations (Figure 8) indicate that the alongshore patterns of profile volume change are linked to offshore wave direction, consistent with observations and simulations for 6–13 October (Figure 3c) and 27–30 October (Figure 4c), and are not strongly affected by the initial bathymetry. In particular, these simulations suggest the formation of the "wedge" after 6 October did not have a dominant effect on the flow divergence and erosion in the wedge area observed between 27 and 30 October. Offshore wave energy larger than observed may cause increased morphologic change, but will not change the sign of the currents.

6. Conclusions

Numerical simulations with a coupled Delft3D/SWAN model for waves, currents, and sediment transport were used to investigate observed surf zone morphologic evolution caused by alongshore-variable forcing and currents resulting from refraction of incident waves over a submarine canyon. The simulations indicate that flow convergences and divergences in a region a few hundred meters from the canyon head depend on the offshore wave direction. Alongshore flow convergence results in net accretion of the cross-shore profile, whereas alongshore flow divergence results in net erosion, consistent with observations. The observations and simulations suggest that bathymetric features on the inner shelf can have first-order effects on nearshore morphologic evolution that depends on the direction of offshore waves.

Acknowledgments
The model used here can be obtained by contacting the corresponding author, and the observational data are available at http://science.whoi.edu/users/elgar/NCEX/ncex.html. Funding was provided by a joint WHOI-USGS postdoctoral scholarship, NSF, ONR, a Vannevar Bush fellowship (ASD(R&E)), NOAA Sea Grant, and the University of Western Australia. We thank Bob Guza for helping to plan and execute the observational program, and the CCS and PVLAB field crews for logistical support. The anonymous reviewers are thanked for their comments and suggestions, which improved the manuscript.

References

Apotsos, A., B. Raubenheimer, S. Elgar, and R. T. Guza (2008), Wave-driven setup and alongshore flows observed onshore of a submarine canyon, *J. Geophys. Res.*, *113*, C07025, doi:10.1029/2007JC004514.

Aubrey, D. G. (1979), Seasonal patterns of onshore/offshore sediment movement, *J. Geophys. Res.*, *84*(C10), 6347–6354, doi:10.1029/JC084iC10p06347.

Aubrey, D. G., D. L. Inman, and C. D. Winant (1980), The statistical prediction of beach changes in southern California, *J. Geophys. Res.*, *85*(C6), 3264–3276, doi:10.1029/JC085iC06p03264.

Bailard, J. A. (1981), An energetics total load sediment transport model for a plane sloping beach, *J. Geophys. Res.*, *86*(C11), 10,938–10,954, doi:10.1029/JC086iC11p10938.

Barnard, P. L., and D. J. Hoover (2010), A seamless, high-resolution coastal digital elevation model (DEM) for southern California, *U.S. Geol. Surv. Data Ser.*, *487*, 8 p. [Available at http://pubs.usgs.gov/ds/487/.]

Battjes, J. A. (1975), Modelling of turbulence in the surf zone, paper presented at Symposium on Modeling Techniques, Am. Soc. of Civ. Eng., San Francisco, Calif.

Bender, C. J., and R. G. Dean (2003), Wave field modification by bathymetric anomalies and resulting shoreline changes: A review with recent results, *Coastal Eng.*, *49*(1-2), 125–153, doi:10.1016/s0378-3839(03)00061-9.

Benedet, L., and J. H. List (2008), Evaluation of the physical process controlling beach changes adjacent to nearshore dredge pits, *Coastal Eng.*, *55*, 1224–1236, doi:10.1016/j.coastaleng.2008.06.008.

Bijker, E. W. (1971), Longshore transport computations, *J. Waterw. Harbors Coastal Eng. Div., Am. Soc. Civ. Eng.*, *97*, 687–701.

Booij, N., R. C. Ris, and L. H. Holthuijsen (1999), A third-generation wave model for coastal regions 1. Model description and validation, *J. Geophys. Res.*, *104*(C4), 7649–7666, doi:10.1029/98JC02622.

Dail, H. J., M. A. Merrifield, and M. Bevis (2000), Steep beach morphology changes due to energetic wave forcing, *Mar. Geol.*, *162*(2–4), 443–458.

Gallagher, E. L., S. Elgar, and R. T. Guza (1998), Observations of sand bar evolution on a natural beach, *J. Geophys. Res.*, *103*(C2), 3203–3215, doi:10.1029/97JC02765.

Gorrell, L., B. Raubenheimer, S. Elgar, and R. T. Guza (2011), SWAN predictions of waves observed in shallow water onshore of complex bathymetry, *Coastal Eng.*, *58*(6), 510–516, doi:10.1016/j.coastaleng.2011.01.013.

Hansen, J. E., E. Elias, and P. L. Barnard (2013), Changes in surfzone morphodynamics driven by multi-decadal contraction of a large ebb-tidal delta, *Mar. Geol.*, *345*, 221–234, doi:10.1016/j.margeo.2013.07.005.

Hansen, J. E., B. Raubenheimer, J. H. List, and S. Elgar (2015), Modeled alongshore circulation and force balances onshore of a submarine canyon, *J. Geophys. Res. Oceans*, *120*, 1887–1903, doi:10.1002/2014JC010555.

Harley, M. D., I. L. Turner, A. D. Short, and R. Ranasinghe (2011), A reevaluation of coastal embayment rotation: The dominance of cross-shore versus alongshore sediment transport processes, Collaroy-Narrabeen Beach, southeast Australia, *J. Geophys. Res.*, *116*, F04033, doi:10.1029/2011JF001989.

Henderson, S. M., J. S. Allen, and P. A. Newberger (2004), Nearshore sandbar migration predicted by an eddy-diffusive boundary layer model, *J. Geophys. Res.*, *109*, C06024, doi:10.1029/2003JC002137.

Hoefel, F., and S. Elgar (2003), Wave-induced sediment transport and sandbar migration, *Science*, *299*(5614), 1885–1887.

Lee, G. H., R. J. Nicholls, and W. A. Birkemeier (1998), Storm-driven variability of the beach-nearshore profile at Duck, North Carolina, USA, 1981-1991, *Mar. Geol.*, *148*(3-4), 163–177.

Lesser, G. R., J. A. Roelvink, J. A. T. M. van Kester, and G. S. Stelling (2004), Development and validation of a three-dimensional morphological model, *Coastal Eng.*, *51*(8–9), 883–915, doi:10.1016/j.coastaleng.2004.07.014.

Lippmann, T. C., and G. M. Smith (2009), Shallow surveying in hazardous waters, paper presented at U.S. Hydrographic Conference (US HYDRO), Center for Coastal and Ocean Mapping, Norfolk, Va.

Long, J. W., and H. T. Özkan-Haller (2005), Offshore controls on nearshore rip currents, *J. Geophys. Res.*, *110*, C12007, doi:10.1029/2005JC003018.

Long, J. W., and H. T. Özkan-Haller (2016), Forcing and variability of nonstationary rip currents, *J. Geophys. Res. Oceans*, *121*, 520–539, doi:10.1002/2015JC010990.

Lygre, A., and H. E. Krogstad (1986), Maximum entropy estimation of the directional distribution in ocean wave spectra, *J. Phys. Oceanogr.*, *16*(12), 2052–2060, doi:10.1175/1520-0485(1986)016 < 2052:MEEOTD>2.0.CO;2.

Magne, R., K. A. Belibassakis, T. H. C. Herbers, F. Ardhuin, W. C. O'Reilly, and V. Rey (2007), Evolution of surface gravity waves over a submarine canyon, *J. Geophys. Res.*, *112*, C01002, doi:10.1029/2005JC003035.

McNinch, J. E. (2004), Geologic control in the nearshore: Shore-oblique sandbars and shoreline erosional hotspots, Mid-Atlantic Bight, USA, *Mar. Geol.*, *211*(1-2), 121–141.

Nipius, K. G. (1998), Transverse transport modelling using Bailard applied to Grevelingenmouth delta, Delft Univ. of Technol., Delft, Netherlands.

Reniers, A. J. H. M., and J. A. Battjes (1997), A laboratory study of longshore currents over barred and non-barred beaches, *Coastal Eng.*, *30*(1–2), 1–21, doi:10.1016/S0378-3839(96)00033-6.

Shi, F., D. M. Hanes, J. T. Kirby, L. Erikson, P. Barnard, and J. Eshleman (2011), Pressure-gradient-driven nearshore circulation on a beach influenced by a large inlet-tidal shoal system, *J. Geophys. Res.*, *116*, C04020, doi:10.1029/2010JC006788.

Sonu, C. J., and J. L. VanBeek (1971), Systematic beach changes on the outer banks, North Carolina, *Geology*, *79*(4), 416–425.

Soulsby, R. L. (1997), *Dynamics of Marine Sands*, Thomas Telford Ltd., London.

Thomson, J., S. Elgar, T. H. C. Herbers, B. Raubenheimer, and R. T. Guza (2007), Refraction and reflection of infragravity waves near submarine canyons, *J. Geophys. Res.*, *112*, C10009, doi:10.1029/2007JC004227.

Thornton, E. B., R. T. Humiston, and W. Birkemeier (1996), Bar/trough generation on a natural beach, *J. Geophys. Res.*, *101*(C5), 12,097–12,110, doi:10.1029/96JC00209.

Van Rijn, L. C. (1993), *Principles of Sedimet Transport in Rivers, Estuaries, and Coastal Seas*, Aqua Publ., Netherlands.

Van Rijn, L. C., D. J. R. Walstra, and M. Ormondt (2004), Description of TRANSPOR2004 and implementation in Delft3-D-ONLINE, *Tech. Rep. Z3748.10*, WL | Delft Hydraul., Delft, Netherlands.

Yates, M. L., R. T. Guza, and W. C. O'Reilly (2009), Equilibrium shoreline response: Observations and modeling, *J. Geophys. Res.*, *114*, C09014, doi:10.1029/2009JC005359.